crystals

MDPI

Article

Synthesis and Structural Analysis of Ternary Ca–Al–Fe Layered Double Hydroxides with Different Iron Contents

Jing Xie [1], Gyeong-Hyeon Gwak [2,3], Minseop Lee [4], Seung-Min Paek [4] and Jae-Min Oh [1,*]

1 Department of Energy and Materials Engineering, Dongguk University-Seoul, Seoul 04620, Korea; jingxie@dongguk.edu
2 Department of Chemistry and Medical Chemistry, College of Science and Technology, Yonsei University, Wonju 220710, Korea; ghgwak@korad.or.kr
3 Korea Radioactive Waste Agency, 19, Chunghyochun-gil, Gyeongju 38033, Korea
4 Department of Chemistry, Kyungpook National University, Daegu 41566, Korea; shlee6697@knu.ac.kr (M.L.); smpaek@knu.ac.kr (S.-M.P.)
* Correspondence: jaemin.oh@dongguk.edu

Abstract: Hydrocalumite structured layered double hydroxides (LDHs) with various Fe^{3+} ratios were prepared through a coprecipitation method. In order to control the Fe^{3+} content in LDH, binary Ca–Fe LDHs were first synthesized with various Ca/Fe ratios. The X-ray diffraction pattern showed that only a limited Ca/Fe ratio resulted in LDH formation. The Fe^{3+} content in LDH was controlled by applying Al^{3+} while the divalent and trivalent metal ratio was set to 2. Through X-ray diffraction patterns, ternary LDHs with Ca–Al–Fe composition were successfully synthesized without significant impurities, with the Al increasing crystallinity. Quantification showed that Al moiety participated in the formation of the LDH framework more than Ca and Fe, implying a structural stabilization in the presence of Al. In order to investigate the global and local structure of Fe moiety in the LDH, both solid state UV-vis and X-ray absorption spectroscopies were carried out. Both spectroscopies revealed that the existence of Al induced slight local distortion in coordination but global crystal stabilization.

Keywords: layered double hydroxide; hydrocalumite; Fe content; Ca/Fe ratio; Ca–Al–Fe ternary LDH

Citation: Xie, J.; Gwak, G.-H.; Lee, M.; Paek, S.-M.; Oh, J.-M. Synthesis and Structural Analysis of Ternary Ca–Al–Fe Layered Double Hydroxides with Different Iron Contents. *Crystals* **2021**, *11*, 1296. https://doi.org/10.3390/cryst11111296

Academic Editor: Giuseppe Prestopino

Received: 20 September 2021
Accepted: 22 October 2021
Published: 26 October 2021

1. Introduction

Layered double hydroxide (LDH) is a family of 2-dimensional layered inorganics having positively charged nanolayers and charge compensating anions [1–4]. LDHs are attracting increasing interest as drug delivery systems [5–8], anionic reservoir/adsorbents [9–12], precursors for catalysts [13–17], catalytic supports [18–20], etc., due to their unique layer-by-layer structure, positive surface charge, anisotropic morphology, and various metal compositions. The general chemical formula of LDH is $M^{2+}_{1-x}M^{3+}_{x}(OH)_2(A^{n-})_{x/n}\cdot mH_2O$, where M^{2+}, M^{3+}, and $A^{n-}\cdot mH_2O$ stand for divalent metal, trivalent metal, and hydrated interlayer anion, respectively. The ratio of M^{2+}/M^{3+} is known to be in the range of 1.5–4.0 with crystallinity lowering being observed at both margins [21]. A layer is composed of $M(OH)_6$ octahedrons having either divalent or trivalent metal ions, and the metal hydroxide units are linked in the crystallographic *ab*-plane direction by sharing each other's edges [22]. Usually, the sizes of divalent and trivalent cations are similar to each other and thus the crystal structure of LDH is similar to that of brucite ($Mg(OH)_2$) [23]. Meanwhile, when Ca^{2+} is involved in the layer structure, there is a slight distortion in the lattice; relatively large Ca^{2+} ions are stabilized in a capped octahedron geometry with a coordination number of 7 [24]. This specific phase of LDH is often referred to as hydrocalumite, in which Ca^{2+}/M^{3+} ratios are set to ~2/1 for structural balance [25–27].

Due to the high biocompatibility, eco-friendliness, and water-soluble properties of Ca–hydroxide, hydrocalumite, i.e., Ca–Al LDH, has been widely studied for biomedical and environmental applications. The Ca–Al LDH has been studied as a Ca-supplement [28],

for nutritional molecule stabilization [29], and as a drug delivery system [30]. On the other hand, wastewater treatment using Ca–Al LDHs has also been reported on consistently; the removal of various water pollutants like B, Mo, Se [31], Cr(VI) [32], and arsenate [33] by Ca–Al LDHs has been studied extensively. Recently, the biomedical and environmental application study on hydrocalumite structure LDH shifted to a Fe-containing material. Various bio-functional moieties, including naproxen [34], antibacterial [35], and even natural extracts [36] were incorporated into Ca–Fe LDHs for potential drug delivery systems. Similarly, in environmental applications, the utilization of Ca–Fe LDHs for water treatment has recently been reported [37,38].

Although there has been much research on the application of Ca–Al or Ca–Fe LDHs, there has been only limited research on the structural properties of Fe-containing hydrocalumite LDH. As far as we know, the structures of Ca–Fe LDHs are less disclosed but different from the composition of Ca–Al LDHs. Kim et al. investigated different coprecipitation behavior of Ca–Fe solution compared with Ca–Al solution and suggested an optimized pH condition to stabilize Ca–Fe LDH [24]. Meanwhile, Sipiczki et al. prepared Ca–Fe LDHs with various ratios and found a difference in $Ca(OH)_2$ impurity and distortion of Fe-hydroxide structure [39]. We hypothesize, in the current research, that the different ionic radius between Al^{3+} (67 pm) and Fe^{3+} (78 pm) influences the structural stabilization of hydrocalumite when Fe^{3+} is substituted for Al^{3+}. In this regard, we aimed to synthesize hydrocalumite-type LDHs with various Fe ratios. First, the Ca/Fe ratio was controlled in a precursor solution to investigate $Ca(OH)_2$ impurity formation and the optimum M^{2+}/M^{3+} ratio for the pure phase. For the next step, the two kinds of trivalent cations, Al^{3+} and Fe^{3+}, were used at various ratios to monitor the structural evolution and local structures. Various spectroscopic analyses, including X-ray diffraction, solid UV-vis spectroscopy and X-ray absorption spectroscopy, were applied to analyze the local and global stabilization of Fe in Ca–Al–Fe LDHs.

2. Materials and Methods

2.1. Synthesis of Binary Ca–Fe LDHs with Various Ca/Fe Ratios

Hydrocalumite-type LDHs were coprecipitated by titrating mixed metal solutions with alkaline solutions. Both calcium nitrate tetrahydrate ($Ca(NO_3)_2 \cdot 4H_2O$) and ferric nitrate nonahydrate ($Fe(NO_3)_3 \cdot 9H_2O$), purchased from Sigma-Aldrich LLC (Saint-Louis, LO, USA), were dissolved in deionized water with various Ca/Fe ratios of 1/1, 2/1, 3/1, 4/1, and 5/1. Alkaline titration with 0.5 mol/L NaOH (Daejung Chemical Co. Ltd. Siheung, Korea) was carried out until the pH reached ~13 for thorough precipitation of metal hydroxide. The suspension was aged for 24 h under vigorous stirring. Then, the precipitate was collected by centrifugation, washed with deionized water, and lyophilized for further characterization. The synthesized LDH with a Ca/Fe ratio of 2/1 was named CAF1 for further comparison.

2.2. Synthesis of Ternary Ca–Al–Fe LDHs with Various Ratios

Synthesis of ternary LDHs with Ca–Al–Fe composition was carried out by precipitation method with various Fe^{3+} contents while the Ca^{2+}/M^{3+} ratio was set to 2/1. Mixed metal solutions containing Ca^{2+}, Al^{3+} ($Al(NO_3)_3 \cdot 9H_2O$ was purchased from Sigma-Aldrich LLC, Saint-Louis, LO, USA), and Fe^{3+} were prepared with different Ca/Al/Fe ratios. The final product with Ca/Al/Fe ratios of 3.33/0.67/1, 4.67/1.33/1, and 5.33/1.67/1, respectively, were named CAF2, CAF3, and CAF4. Each metal solution was titrated by alkaline solution until pH~13. After the reaction for 24 h, the precipitates were centrifugated, washed, and lyophilized.

2.3. Characterization

The crystal structure of the synthesized samples was first analyzed by powder X-ray diffractometer (XRD, 2D Phaser, Bruker AXS GmbH, Kalsruhe, Germany). The local structure around the Ca and Fe was investigated by X-ray absorption fine structure (XAFS) at

8C NanoXAFS beamline in Pohang Accelerator Laboratory (PAL), Pohang, Korea. X-ray absorption near edge structure (XANES) and extended X-ray absorption fine structure (EXAFS) spectra of Ca K-edge and Fe K-edge were obtained in transmission mode. XANES spectra were normalized with default parameters by Athena software. Fourier transformed EXAFS spectra data were not phase shift corrected. The electronic spectra were examined by measuring solid state UV-vis spectroscopy (EVOLUTION 220, ThermoFisher Scientific, Waltham, MA, USA). The chemical composition of obtained LDHs was determined by inductively coupled plasma-optical emission spectroscopy (ICP-OES, Optima 8300, PerkinElmer, Waltham, MA, USA) after digestion in hydrochloric acid. The microstructures of the Ca–Fe LDHs and Ca–Al–Fe LDHs were visualized by scanning electron microscopy (SEM) with JSM-6700F (JEOL). The measured sample was prepared by tenderly spreading the LDH powder on carbon tapes.

3. Results and Discussion

3.1. X-ray Diffraction (XRD) Analysis

According to the XRD patterns of Ca–Fe LDHs with nominal Ca/Fe ratios of 1, 2, 3, 4, and 5 (Figure 1), it was confirmed that the pure hydrocalumite phase could be obtained with a certain Ca/Fe ratio range. As shown in Figure 1a,b, the LDHs with nominal Ca/Fe ratios of 1/1 and 2/1 showed a well-developed hydrocalumite structure intercalated with NO_3^- (JCPDS No. 48-0065) [40]. With a higher Ca/Fe ratio, we could observe dual phases of hydrocalumite and $Ca(OH)_2$. In order to quantitatively analyse the lattice dimensions of Ca–Fe LDHs depending on the nominal Ca/Fe ratios, the lattice parameters of the LDHs were calculated utilizing all the diffraction peaks and are summarized in Table 1. It was notable that the lattice parameter values were the same as each other regardless of the nominal Ca/Fe ratio. The result suggested that the Ca–Fe hydrocalumites were obtained from a common crystal structure, although there was a $Ca(OH)_2$ impurity with an increasing Ca/Fe nominal ratio. The discrepancy in c values and basal spacings with respect to Ca/Fe ratio did not mean a difference in crystal structure. It is rather attributed to the water content in the interlayer space according to previous reports that describes the relationship between basal spacing and water content in clay materials [41,42]. Upon increasing Ca content in the starting metal solution, impurity phases appeared obviously (Figure 1c,d). The intense impurity peaks observed at 2~18° and ~34° are attributed to the reflection along (001) and (101), respectively, of the $Ca(OH)_2$. The intensity of the diffraction peak for $Ca(OH)_2$ gradually increased upon increasing Ca content in the starting solution. This result indicated that only a limited amount of Ca^{2+} was incorporated into the Ca–Fe LDH lattice and that the remaining Ca^{2+} moiety precipitated as the $Ca(OH)_2$ phase. This result is consistent with previous research [39], which reported the formation of $Ca(OH)_2$ to stabilize hydrocalumite structure within the optimized Ca^{2+}/Fe^{3+} ratio of ~2 when an excessive amount of Ca^{2+} was present in the starting solution. Through the XRD analyses, we could suggest that the M^{2+}/M^{3+} ratio should be maintained between 1 and 2 in the precursor solution to gain pure hydrocalumite phased LDH.

In order to vary the Fe content in the LDH structure, mixed metal solutions containing diverse ratios of Ca/Al/Fe were utilized as precursors for Ca–Al–Fe LDH, while the Ca^{2+}/M^{3+} ratio was set to 2/1. Lattice constants *a* and *c* of Ca–Al–Fe LDHs were calculated with all the observed diffraction peaks and listed in Table 2. A slight decreasing pattern in lattice parameter *a* in CAFs were observed from 6.0 Å to 5.8 Å with increasing Al, which was attributed to both the difference in ionic radius between Al^{3+} and Fe^{3+} and total metal ratio (Table 3). The d-values along the (002) plane of CAF1, CAF2, CAF3, and CAF4 were 8.4 Å, 8.8 Å, 8.7 Å, and 8.7 Å, respectively. Even though all of the prepared LDHs had the same intercalated anion of NO_3^-, there was a discrepancy in parameter *c* and basal spacing of the prepared LDHs, which was attributed to water content in the inter-layer space [41,42]. As shown in Figure 2, all the samples showed a well-developed hydrocalumite phase without significant impurities regardless of Ca/Al/Fe ratios in the starting solution. The crystallinity became higher with increased Al content. For a semi-quantitative analysis

of the crystallinity change, the crystallinity (ordered domain) along the crystallographic *c*-axis and *ab*-plane direction were calculated by the Scherrer's equation (t = (0.9λ)/(Bcosθ), t: ordered domain, λ: X-ray wavelength, B: full-width at half-maximum (FWHM)). The FWHM values of (002) peaks were 0.7°, 0.5°, 0.4°, and 0.4° for CAF1, CAF2, CAF3, and CAF4, respectively, matching the range of ordered domain 11 nm, 17 nm, 20 nm, and 20 nm, respectively, in the c-axis direction. The FWHM values of (110) were 0.3°, 0.3 °, 0.2°, and 0.3° for CAF1, CAF2, CAF3, and CAF4, respectively, resulting in ordered domain sizes of 26 nm, 33 nm, 36 nm, and 32 nm, respectively. This result clearly showed that the crystallinity of Ca–Al–Fe LDH increased in the presence of Al. In other words, the lattice structure became more stable with both Al^{3+} and Fe^{3+} in the hydrocalumite layer than with Fe^{3+} alone. Additionally, it is recommended that a ternary composition is prepared in order to stabilize Fe^{3+} in the Ca–Al–Fe LDH structure.

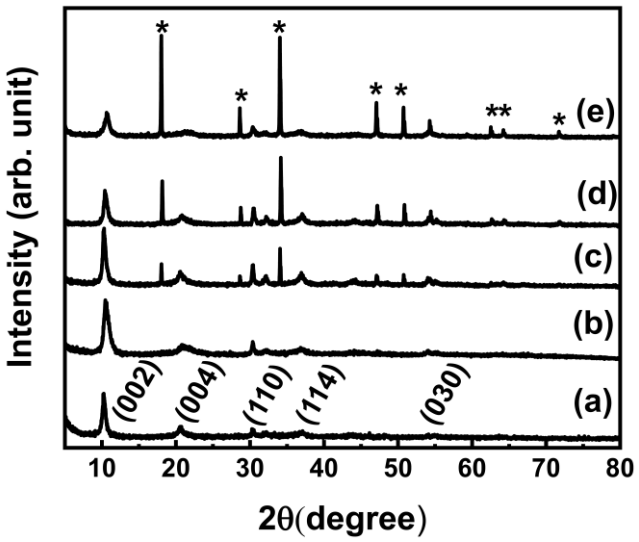

Figure 1. XRD patterns for Ca–Fe LDHs with various nominal Ca/Fe ratios of (**a**) 1, (**b**) 2, (**c**) 3, (**d**) 4, and (**e**) 5. * stands for the $Ca(OH)_2$ impurity.

Table 1. Structural parameters of the synthesized materials.

Nominal Ca/Fe Ratio	Lattice Parameters		Basal Spacing (Å)
	a (Å)	*c* (Å)	
1	6.0	17.4	8.7
2	6.0	17.0	8.4
3	6.0	17.3	8.6
4	6.0	17.1	8.4
5	6.0	17.0	8.4

Table 2. Structural parameters of the synthesized materials.

Samples	Lattice Parameters		Basal Spacing (Å)
	a (Å)	*c* (Å)	
CAF1	6.0	16.9	8.4
CAF2	5.9	17.2	8.8
CAF3	5.8	16.9	8.7
CAF4	5.8	16.9	8.7

Table 3. Quantitative data on Ca–Al–Fe LDHs. Nominal (nom.) and actual (act.) ratios stand for molar metal ratios in starting solution and the values calculated from ICP-OES, respectively. M_{tot} indicates the total metal contents including Ca, Al, and Fe.

Sample	Nominal Ratio			Actual Ratio			Ca^{2+}/M_{tot}		Al^{3+}/M_{tot}		Fe^{3+}/M_{tot}		$Ca^{2+}/(Al^{3+}+Fe^{3+})$		Fe wt%
	Ca	Al	Fe	Ca	Al	Fe	nom.	act.	nom.	act.	nom.	act.	nom.	act.	
CAF1	2.00	0.00	1.00	2.44	0.00	1.00	0.67	0.71	0.00	0.00	0.33	0.29	2.00	2.44	23.07
CAF2	3.33	0.67	1.00	3.30	1.41	1.00	0.67	0.58	0.13	0.25	0.20	0.18	2.00	1.37	14.14
CAF3	4.67	1.33	1.00	4.11	2.68	1.00	0.67	0.53	0.19	0.34	0.14	0.13	2.00	1.12	10.43
CAF4	5.33	1.67	1.00	4.97	3.34	1.00	0.67	0.53	0.21	0.36	0.13	0.11	2.00	1.15	8.82

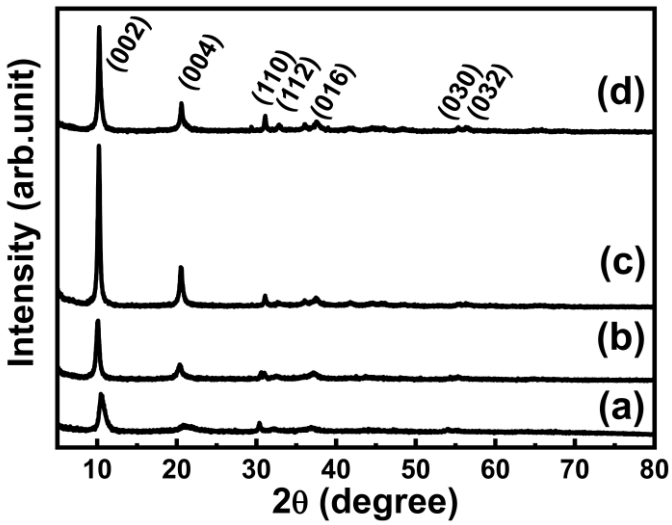

Figure 2. XRD patterns of Ca–Al–Fe LDHs with various Ca/Al/Fe ratios (**a**) CAF1, (**b**) CAF2, (**c**) CAF3, and (**d**) CAF4.

3.2. Quantification of Ca/Al/Fe Ratios in CAF Samples

The actual Ca/Al/Fe ratios in CAF samples were evaluated with ICP-OES and compared with the nominal metal ratios (Table 3). We could clearly observe a discrepancy between the nominal and actual ratios. First of all, the CAF1, in which only Ca^{2+} and Fe^{3+} were utilized, showed slightly higher Ca^{2+} and lower Fe^{3+} content in LDH than in the precursor solution (see Ca^{2+}/M_{tot} and Fe^{3+}/M_{tot} value). This result showed that Fe^{3+} was preferentially precipitated compared with Ca^{2+} at a coprecipitation pH~13. We also investigated the difference between nominal and actual metal ratios upon the addition of Al^{3+}. The content of a certain metal species over total (Ca^{2+}/M_{tot}, Al^{3+}/M_{tot}, and Fe^{3+}/M_{tot}) exhibited that both Ca and Fe content in LDH decreased compared with the value in the precursor metal solution. On the other hand, the Al content was larger in LDH products than in the metal solution. More quantitatively, the Fe/M_{tot} and Ca/M_{tot} ratio decreased in the range of 85–93% and 79–87%, respectively, while the Al/M_{tot} ratio increased within the 171–192% range. We could see two interesting points in the quantification data. First, metal cations participated in a precipitation reaction with different efficiencies when several cations were mixed together, and the tendency of participation was in the order Al>Fe>Ca. Second, the degree of participation in the precipitation reaction did not change significantly at different metal ratios. The former finding suggested that Al^{3+} was the best stabilized in the metal hydroxide framework, and the latter implied that the Fe^{3+} was well distributed in the LDH lattice without serious waste during the reaction. Although we could not preserve the metal ratios of the starting solution in the final CAF samples, the data proposed how to control Fe content in the LDH structure (Fe wt% values in Table 3).

3.3. Solid State UV/Vis Spectroscopy of CAF Samples

In order to estimate the electronic structure of Fe^{3+} ions in the LDH lattice, solid state UV-vis spectra were measured (Figure 3a). The absorption of $Fe(III)(OH)_6$ was strongly found in the UV region and widely found in the visible regions with a wavelength range of 400–600 nm. As the Fe^{3+} in hydroxide lattice has a $t_{2g}{}^3e_g{}^2$ electronic structure, the d–d transition is spin-forbidden, and only ligand to metal electron transfer (LMCT) accounts for the visible light absorption [43]. The intensity in the wavelength 400–600 nm region was the largest in binary Ca–Fe LDH (CAF1), while the peak intensities of ternary Ca–Al–Fe LDHs (CAF2, 3, and 4) were fairly comparable to each other. The result is different from the general expectation that the visible light absorption was dependent on Fe contents. As shown in Table 3, the weight% values for Fe^{3+} in CAF1, 2, 3, and 4 were 23.1wt%, 14.1wt%, 10.4wt%, and 8.8wt%, respectively. The Fe^{3+} content and absorption (400–600 nm) intensity were not linear in ternary Ca–Al–Fe LDH. In spite of lower Fe^{3+} content in CAF3 than in CAF2, it showed slightly higher absorption at around 500 nm. Similarly, CAF4, which has the lowest Fe^{3+} content, showed comparable absorption intensity with CAF2 and CAF3. This result indicated that LMCT around Fe^{3+} in ternary Ca–Al–Fe LDH was facilitated with low Fe^{3+} content. It was previously reported that the local distortion or ligand vacancy in metal hydroxide increased the number of photons involved in charge transfers [44,45]. Although the XRD data (Figure 2) showed higher crystallinity with lower Fe content in CAFs, the UV-vis spectroscopy suggested that the local structure around Fe could be distorted. It should be noted, however, that the distorted local structure does not stand for the instability of Fe within the LDH layer. Instead, it can be concluded that the Fe^{3+} was evenly distributed throughout the globally crystallized Ca–Al–Fe LDH lattice with slight local distortions.

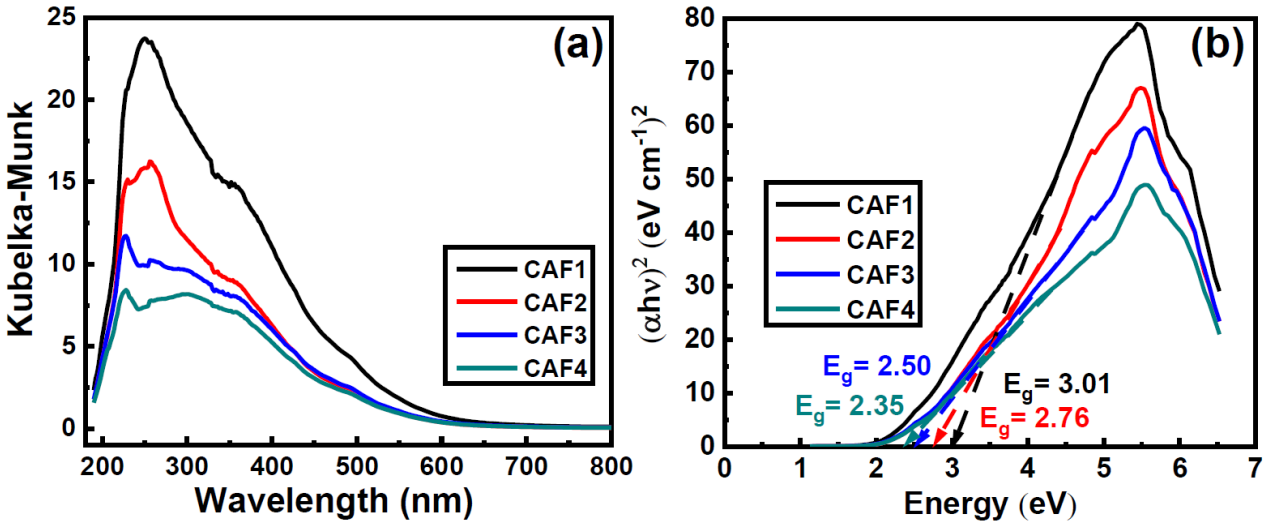

Figure 3. (**a**) Solid state UV-vis spectra and (**b**) Tauc plot of Ca–Al–Fe LDHs with various Ca/Al/Fe ratios.

The energy gap between the valence band and conduction band (band-gap) was calculated using the Tauc function, with values of 3.01, 2.76, 2.50, and 2.35 eV for CAF1, CAF2, CAF3, and CAF4, respectively (Figure 3b). The band-gap values are highly related to the macroscopic structure such as overall ordering, particle size, degree of unsaturated coordination, etc. In the previous study on perovskite materials, the global distortion in the crystal structure increased the band-gap [46,47]. Furthermore, small size and impurity tended to increase the band-gap [48–50]. The smaller band-gap with increasing Al^{3+} (decreasing Fe^{3+}) indicated that the lattice structure of LDH near Fe was stable and pure in the presence of Al. Taking into account the XRD and UV-vis spectroscopy, we can conclude that the Al^{3+} is a crucial element to stabilize Fe-containing hydrocalumites.

3.4. X-ray Absorption Fine Structure (XAFS)

Local structure of CAFs around Ca and Fe cations was evaluated by X-ray absorption spectroscopy (XAS). First, the XANES spectra of Ca K-edge were investigated as Ca is the most abundant metal cation in the CAF framework. As shown in Figure 4, all four XANES spectra showed two-step absorption: pre-edge peak and main edge attributed to 1s→3d and 1s→4p transition, respectively [24]. The main edge position of Ca K-edge spectra is known to be strongly related to the coordination number of Ca; the main edge energy increases with an increasing coordination number around Ca [51,52]. The main edge of the Ca K-edge was similar in all the CAF samples, at 4040.6, 4040.9, 4040.9, and 4040.7 eV for CAF1, CAF2, CAF3, and CAF4, respectively. This result implied that the local structure of CAFs around Ca^{2+} ions was not significantly affected by the distribution of Al^{3+} and Fe^{3+} cation. It is parallel to the result that the Ca/M_{tot} ratios were not notably different from each other in CAFs regardless of Ca/Al/Fe ratios.

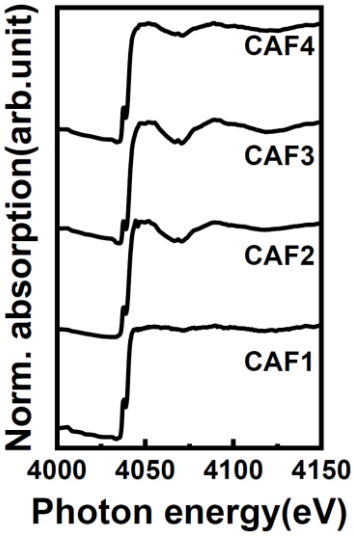

Figure 4. Ca K-edge XANES spectra for Ca–Al–Fe LDHs with various Ca/Al/Fe ratios.

The Fe K-edge XANES was also checked to confirm the local structure of CAFs around Fe^{3+} cations. As shown in the left panel of Figure 5, the XANES spectra of all the CAFs were fairly similar in terms of peak shape and intensity, suggesting the chemical environments around Fe^{3+} were fairly similar to each other in CAFs. However, a closer look at the pre-edge region (right panel of Figure 5) revealed that the increasing Al^{3+} content resulted in an enhancement of pre-edge. As is well known, the pre-edge and main edge of Fe K-edge XANES are attributed to 1s→3d and 1s→4p transitions, respectively [53]. The La Porte forbidden 1s→3d transition is allowed when the symmetry around metal ions is distorted. It is known that Fe in LDH is stabilized in the octahedral center; in fact, however, the octahedrons have rather D_{4h} than O_h symmetry [21,39]. Due to the size difference between Al^{3+} (67 pm) and Fe^{3+} (78 pm in high spin configuration), the local structure around Fe^{3+} could be distorted. This finding is in parallel with the facilitated LMCT phenomena in ternary LDH, as discussed with regard to the solid UV-vis spectroscopy (Figure 3). In addition, it is also interesting that the main edge position of Fe K-edge was slightly different with different Al^{3+} content. The calculated main edge positions were 7129.5, 7128.5, 7127.4, and 7127.4 eV for CAF1, CAF2, CAF3, and CAF4, respectively. Decreasing main edge position according to increasing Al^{3+} would be interpreted by the shielding theory. As Al^{3+} is small and hard acid, it can attract electron density; consequently, electron density of OH^- coordinated to Fe^{3+} would be reduced by the neighboring Al^{3+}. As Al^{3+} content increases, electrons in Fe^{3+} would experience less shielding and less energy is required for the 1s→4p transition.

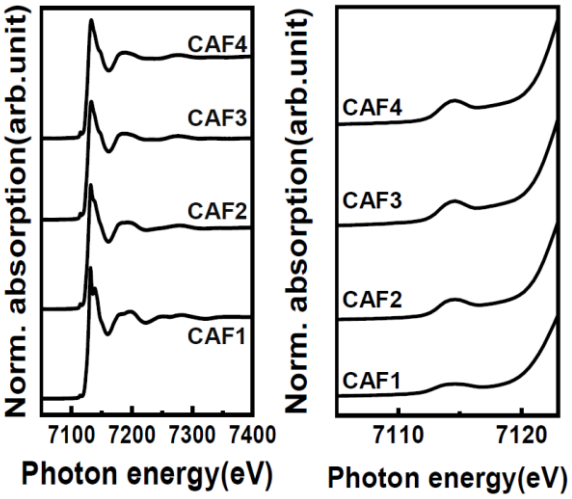

Figure 5. Fe K-edge XANES spectra for Ca–Al–Fe LDHs with various Ca/Al/Fe ratios (right panel shows magnified spectra around pre-edge region).

As we found a slight difference in the chemical environment around Fe, we further analyzed EXAFS spectra for all CAFs shown in Figure 6. Obviously, the first shell Fe–O distance appeared at 1.5Å (non-phase-shift-corrected) for all the CAFs. However, the position of Fe–O in CAF4 shifted to the shorter region, while the second shell of ternary LDHs (CAF2, CAF3, and CAF4) was located in a shorter position than binary LDH (CAF1). There was no significant difference in the structure of the second shell, where the position of calcium ions is modulated by the intercalated anions and contributes to the NO_3^- anions. The notable difference can be found in the third shell. The calcium ions of CAF1 lay the furthest from the Fe(III) ion (3.11–3.13 Å) and the other three had a smaller distance to Fe(III), attributed to calcium content.

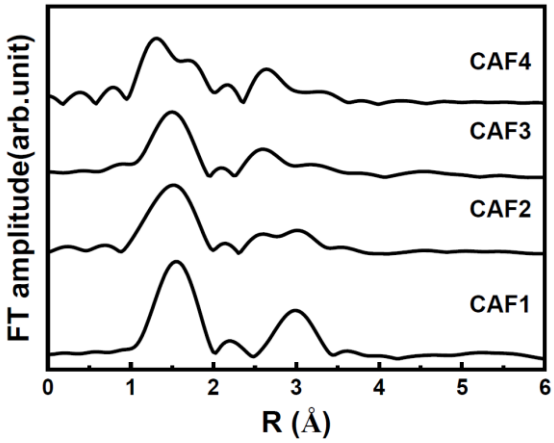

Figure 6. Fe K-edge EXAFS spectra for Ca–Al–Fe LDHs with various Ca/Al/Fe ratios.

3.5. Electron Microscopy Study of the As-Prepared Ca–Fe LDH and Ca–Al–Fe LDH Samples

The morphology of the as-prepared Ca–Fe LDHs with Ca/Fe ratios of 2, 3, and 4, and Ca–Al–Fe LDHs with Ca/Al/Fe ratios of 8/1/3 and 5/1/1.5 were evaluated by SEM, as shown in Figures 7 and 8, respectively. The Ca–Fe LDH with a Ca/Fe ratio of 2 performed randomly assembled platelet-like particles (Figure 7a), suggesting that it was hydrocalumite. The average lateral dimension and thickness of that were 400 nm and 30 nm, respectively. However, the platelet-like and granular particles of the Ca–Fe LDH with a Ca/Fe ratio of 3 and 4 were observed (Figure 7b,c), and we suspected that the hydrocalumite and other impurities coexisted, suggesting that $Ca(OH)_2$ was one of the impurity candidates, which was confirmed by the results from XRD. Moreover, the

morphologies of granular agglomeration and platelets were evident in Ca–Al–Fe LDHs with Ca/Al/Fe ratios of 8/1/3 and 5/1/1.5, respectively (Figure 8). Notably, there was only a single-phase generated in Ca–Al–Fe LDHs with Ca/Al/Fe ratios of 8/1/3 and 5/1/1.5, consistent with the XRD data shown in Figure 2.

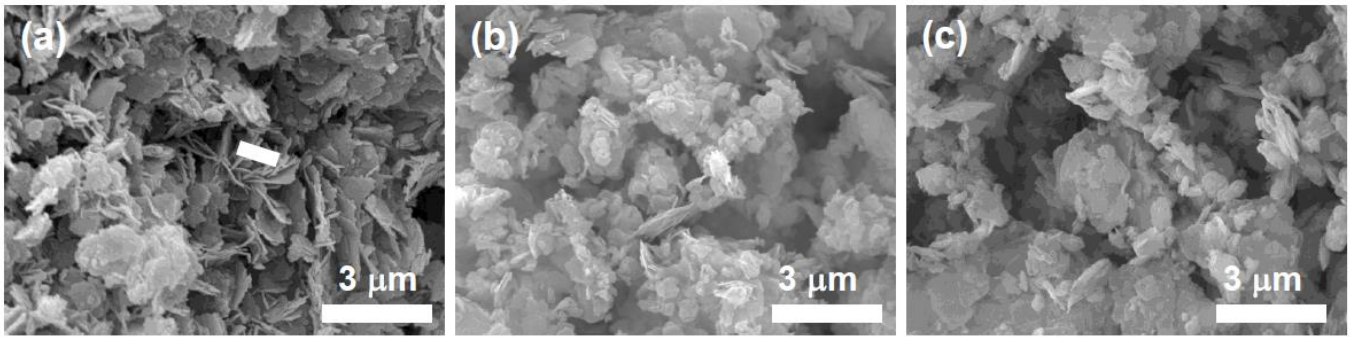

Figure 7. SEM images for CaFe LDHs with Ca/Fe ratios of (**a**) 2, (**b**) 3, (**c**) 4.

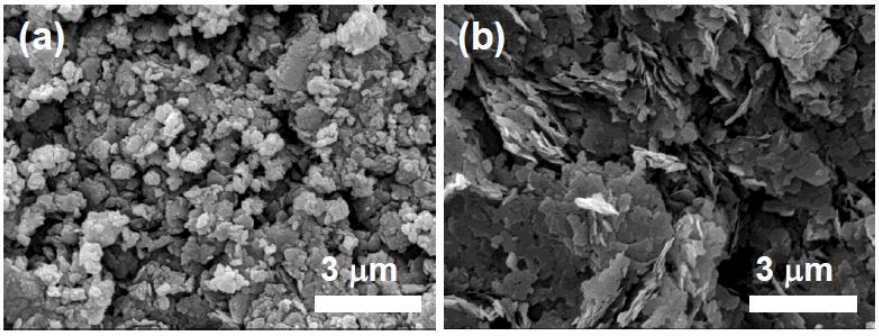

Figure 8. SEM images of Ca–Al–Fe LDH with Ca/Al/Fe ratios of (**a**) 8:1:3 and (**b**) 5:1:1.5.

4. Conclusions

The structure and composition of hydrocalumite type LDH with Ca–Al–Fe composition were investigated in this study. It was confirmed that pure binary LDH with Ca–Fe composition could only be obtained with a limited metal ratio of 2/1. XRD analyses confirmed that excessive Ca moiety in precursor solution resulted in a mixed phase with $Ca(OH)_2$. In order to introduce Fe^{3+} in hydrocalumite type LDH at various ratios, ternary Ca–Al–Fe LDH with various metal ratios were prepared. The XRD analyses showed that the crystallinity became higher with increasing Al moiety while there existed Ca moiety, which did not participate in precipitation reactions in the presence of Al. The band-gap calculation from solid state UV-vis spectroscopy suggested that the global crystallinity and ordering around Fe were higher in the presence of Al in the LDH framework. On the other hand, the LMCT phenomena in solid state UV-vis spectra and X-ray absorption spectra suggested that local the structure around Fe could be slightly distorted in the presence of Al in the LDH framework. This local distortion was attributed to the size mismatch between Fe and Al, and it did not seriously affect the stable incorporation of Fe in the LDH framework. It can be concluded that the Fe moiety could be stably incorporated in a well-crystallized hydrocalumite type LDH framework when Al coexisted with Fe and Ca.

Author Contributions: Conceptualization, J.X. and J.-M.O.; methodology, G.-H.G., M.L. and S.-M.P.; software, J.X. and G.-H.G.; validation, G.-H.G., M.L. and S.-M.P.; formal analysis, J.X.; investigation, J.X., G.-H.G., M.L. and S.-M.P.; resources, M.L. and S.-M.P.; data curation, J.X. and G.-H.G.; writing—original draft preparation, J.X.; writing—review and editing, J.-M.O.; visualization, J.X. and G.-H.G.; supervision, J.-M.O.; project administration, J.-M.O.; funding acquisition, J.-M.O. All authors have read and agreed to the published version of the manuscript.

Funding: This work was supported by a grant from the International Research & Development Program (2020K1A3A1A21039816) through the National Research Foundation of Korea (NRF) funded by the Ministry of Science, ICT, and Future Planning, Korea.

Institutional Review Board Statement: Not applicable.

Informed Consent Statement: Not applicable.

Data Availability Statement: Data underlying the results presented in this paper are not publicly available at this time but may be obtained from the authors upon reasonable request.

Acknowledgments: The fabrication processes in this work were supported by the Nano-Bio Materials Lab.

Conflicts of Interest: The authors declare no conflict of interest.

References

1. Chaillot, D.; Bennici, S.; Brendlé, J. Layered double hydroxides and LDH-derived materials in chosen environmental applications: A review. *Environ. Sci. Pollut. Res.* **2021**, *28*, 24375–24405. [CrossRef]
2. Oh, J.M.; Choi, S.J.; Lee, G.E.; Kim, J.E.; Choy, J.H. Inorganic metal hydroxide nanoparticles for targeted cellular uptake through clathrin-mediated endocytosis. *Chem. Asian J.* **2009**, *4*, 67–73. [CrossRef] [PubMed]
3. Baikousi, M.; Stamatis, A.; Louloudi, M.; Karakassides, M.A. Thiamine pyrophosphate intercalation in layered double hydroxides (LDHs): An active bio-hybrid catalyst for pyruvate decarboxylation. *Appl. Clay Sci.* **2013**, *75–76*, 126–133. [CrossRef]
4. Li, C.; Wei, M.; Evans, D.G.; Duan, X. Layered double hydroxide-based nanomaterials as highly efficient catalysts and adsorbents. *Small* **2014**, *10*, 4469–4486. [CrossRef] [PubMed]
5. Ladewig, K.; Zhi, P.X.; Gao, Q.L. Layered double hydroxide nanoparticles in gene and drug delivery. *Expert Opin. Drug Deliv.* **2009**, *6*, 907–922. [CrossRef] [PubMed]
6. Bi, X.; Zhang, H.; Dou, L. Layered double hydroxide-based nanocarriers for drug delivery. *Pharmaceutics* **2014**, *6*, 298–332. [CrossRef] [PubMed]
7. Kim, H.J.; Jeung, D.G.; Oh, J.M. Boosting the anticancer activity of doxorubicin with a layered double hydroxide nanocarrier. *Appl. Clay Sci.* **2021**, *203*, 106000. [CrossRef]
8. Ryu, S.J.; Jung, H.; Oh, J.M.; Lee, J.K.; Choy, J.H. Layered double hydroxide as novel antibacterial drug delivery system. *J. Phys. Chem. Solids* **2010**, *71*, 685–688. [CrossRef]
9. Daud, M.; Hai, A.; Banat, F.; Wazir, M.B.; Habib, M.; Bharath, G.; Al-Harthi, M.A. A review on the recent advances, challenges and future aspect of layered double hydroxides (LDH)–Containing hybrids as promising adsorbents for dyes removal. *J. Mol. Liq.* **2019**, *288*, 110989. [CrossRef]
10. Wang, J.; Zhang, T.; Li, M.; Yang, Y.; Lu, P.; Ning, P.; Wang, Q. Arsenic removal from water/wastewater using layered double hydroxide derived adsorbents, a critical review. *RSC Adv.* **2018**, *8*, 22694–22709. [CrossRef]
11. Goh, K.H.; Lim, T.T.; Dong, Z. Application of layered double hydroxides for removal of oxyanions: A review. *Water Res.* **2001**, *42*, 1343–1368. [CrossRef] [PubMed]
12. Xie, J.; Yamaguchi, T.; Oh, J.M. Synthesis of a mesoporous Mg–Al–mixed metal oxide with P123 template for effective removal of Congo red via aggregation-driven adsorption. *J. Solid State Chem.* **2021**, *293*, 121758. [CrossRef]
13. Xu, M.; Wei, M. Layered double hydroxide-based catalysts: Recent advances in preparation, structure, and applications. *Adv. Funct. Mater.* **2018**, *28*, 1802943. [CrossRef]
14. He, S.; An, Z.; Wei, M.; Evans, D.G.; Duan, X. Layered double hydroxide-based catalysts: Nanostructure design and catalytic performance. *Chem. Commun.* **2013**, *49*, 5912–5920. [CrossRef] [PubMed]
15. Verónica, M.; Graciela, B.; Norma, A.; Miguel, L. Ethanol steam reforming using Ni(II)-Al(III) layered double hydroxide as catalyst precursor. Kinetic study. *Chem. Eng. J.* **2008**, *138*, 602–607. [CrossRef]
16. Li, F.; Tan, Q.; Evans, D.G.; Duan, X. Synthesis of carbon nanotubes using a novel catalyst derived from hydrotalcite-like Co-Al layered double hydroxide precursor. *Catal. Lett.* **2005**, *99*, 151–156. [CrossRef]
17. Chen, G.; Gao, R.; Zhao, Y.; Li, Z.; Waterhouse, G.I.N.; Shi, R.; Zhao, J.; Zhang, M.; Shang, L.; Sheng, G.; et al. Alumina-supported CoFe alloy catalysts derived from layered-double-hydroxide nanosheets for efficient photothermal CO_2 hydrogenation to hydrocarbons. *Adv. Mater.* **2018**, *30*, 1704663. [CrossRef]
18. Zhang, H.; Qi, R.; Evans, D.G.; Duan, X. Synthesis and characterization of a novel nano-scale magnetic solid base catalyst involving a layered double hydroxide supported on a ferrite core. *J. Solid State Chem.* **2004**, *177*, 772–780. [CrossRef]
19. Zhang, M.; Yao, Q.; Guan, W.; Lu, C.; Lin, J.M. Layered double hydroxide-supported carbon dots as an efficient heterogeneous Fenton-like catalyst for generation of hydroxyl radicals. *J. Phys. Chem. C* **2014**, *118*, 10441–10447. [CrossRef]
20. de Rezende, S.M.; Franchini, C.A.; Dieuzeide, M.L.; Duarte de Farias, A.M.; Amadeo, N.; Fraga, M.A. Glycerol steam reforming over layered double hydroxide-supported Pt catalysts. *Chem. Eng. J.* **2015**, *272*, 108–118. [CrossRef]
21. Rives, V. *Layered Double Hydroxides: Present and Future*; Nova Science Publishers, Inc.: New York, NY, USA, 2001.
22. Mota, L.; Sorg, I.; Cornelis, G.; Parsot, C.; Bach, S.; Stanford, K.; McAllister, T.; Cheng, H.; Jiang, N.; Shen, A. *Structure and Bonding*; Sprinter: Berlin/Heidelberg, Germany, 2005; Volume 252, ISBN 9783540282792.

23. Zhi, P.X.; Guo, Q.L. Hydrothermal synthesis of layered double hydroxides (LDHs) from mixed MgO and Al_2O_3: LDH formation mechanism. *Chem. Mater.* **2005**, *17*, 1055–1062. [CrossRef]
24. Kim, T.H.; Heo, I.; Paek, S.M.; Park, C.B.; Choi, A.J.; Lee, S.H.; Choy, J.H.; Oh, J.M. Layered metal hydroxides containing calcium and their structural analysis. *Bull. Korean Chem. Soc.* **2012**, *33*, 1845–1850. [CrossRef]
25. Kalinichev, A.G.; Kirkpatrick, R.J.; Cygan, R.T. Molecular modeling of the structure and dynamics of the interlayer and surface species of mixed-metal layered hydroxides: Chloride and water in hydrocalumite (Friedel's salt). *Am. Mineral.* **2000**, *85*, 1046–1052. [CrossRef]
26. Muráth, S.; Szabados, M.; Sebők, D.; Kukovecz, Á.; Kónya, Z.; Szilágyi, I.; Sipos, P.; Pálinkó, I. Influencing the texture and morphological properties of layered double hydroxides with the most diluted solvent mixtures—The effect of 6–8 carbon alcohols and temperature. *Colloids Surf. A Physicochem. Eng. Asp.* **2019**, *574*, 146–153. [CrossRef]
27. Rousselot, I.; Taviot-Guého, C.; Leroux, F.; Léone, P.; Palvadeau, P.; Besse, J.P. Insights on the structural chemistry of hydrocalumite and hydrotalcite-like materials: Investigation of the series $Ca_2M^{3+}(OH)_6Cl{\cdot}2H_2O$ (M^{3+}: Al^{3+}, Ga^{3+}, Fe^{3+}, and Sc^{3+}) by X-ray powder diffraction. *J. Solid State Chem.* **2002**, *167*, 137–144. [CrossRef]
28. Kim, T.H.; Lee, J.A.; Choi, S.J.; Oh, J.M. Polymer coated CaAl-layered double hydroxide nanomaterials for potential calcium supplement. *Int. J. Mol. Sci.* **2014**, *15*, 22563–22579. [CrossRef]
29. Kim, T.H.; Oh, J.M. Dual nutraceutical nanohybrids of folic acid and calcium containing layered double hydroxides. *J. Solid State Chem.* **2016**, *233*, 125–132. [CrossRef]
30. Shahabadi, N.; Razlansari, M.; Zhaleh, H.; Mansouri, K. Antiproliferative effects of new magnetic pH-responsive drug delivery system composed of Fe_3O_4, CaAl layered double hydroxide and levodopa on melanoma cancer cells. *Mater. Sci. Eng. C* **2019**, *101*, 472–486. [CrossRef] [PubMed]
31. Zhang, M.; Reardon, E.J. Removal of B, Cr, Mo, and Se from wastewater by incorporation into hydrocalumite and ettringite. *Environ. Sci. Technol.* **2003**, *37*, 2947–2952. [CrossRef] [PubMed]
32. Periyasamy, S.; Viswanathan, N. Hydrothermal synthesis of hydrocalumite assisted biopolymeric hybrid composites for efficient Cr(VI) removal from water. *New J. Chem.* **2018**, *42*, 3371–3382. [CrossRef]
33. Grover, K.; Komarneni, S.; Katsuki, H. Synthetic hydrotalcite-type and hydrocalumite-type layered double hydroxides for arsenate uptake. *Appl. Clay Sci.* **2010**, *48*, 631–637. [CrossRef]
34. Szabados, M.; Gácsi, A.; Gulyás, Y.; Kónya, Z.; Kukovecz, Á.; Csányi, E.; Pálinkó, I.; Sipos, P. Conventional or mechanochemically-aided intercalation of diclofenac and naproxen anions into the interlamellar space of CaFe-layered double hydroxides and their application as dermal drug delivery systems. *Appl. Clay Sci.* **2021**, *212*, 106233. [CrossRef]
35. Gopala Kumari, S.V.; Manikandan, N.A.; Pakshirajan, K.; Pugazhenthi, G. Sustained drug release and bactericidal activity of a novel, highly biocompatible and biodegradable polymer nanocomposite loaded with norfloxacin for potential use in antibacterial therapy. *J. Drug Deliv. Sci. Technol.* **2020**, *59*, 101900. [CrossRef]
36. Jung, S.Y.; Kim, H.J.; Oh, J.M. Synthetic mineral containing Sr, Ca, and Fe and its hybridization with soybean extract for synergetic bone regeneration. *Mater. Chem. Phys.* **2020**, *255*, 123620. [CrossRef]
37. Al Jaberi, M.; Mallet, M.; Greenwell, H.C.; Abdelmoula, M.; Ruby, C. Using Ca–Fe layered double hydroxide transformation to optimise phosphate removal from waste waters. *Appl. Clay Sci.* **2019**, *182*, 105281. [CrossRef]
38. Park, J.Y.; Lee, J.; Go, G.M.; Jang, B.; Cho, H.B.; Choa, Y.H. Removal performance and mechanism of anti-eutrophication anions of phosphate by CaFe layered double hydroxides. *Appl. Surf. Sci.* **2021**, *548*, 149157. [CrossRef]
39. Sipiczki, M.; Kuzmann, E.; Homonnay, Z.; Megyeri, J.; Pálinkó, I.; Sipos, P. The structure and stability of CaFe layered double hydroxides with various Ca:Fe ratios studied by Mössbauer spectroscopy, X-ray diffractometry and microscopic analysis. *J. Mol. Struct.* **2013**, *1044*, 116–120. [CrossRef]
40. Al-Jaberi, M.; Naille, S.; Dossot, M.; Ruby, C. Interlayer interaction in Ca–Fe layered double hydroxides intercalated with nitrate and chloride species. *J. Mol. Struct.* **2015**, *1102*, 253–260. [CrossRef]
41. Michaelaicken, B.A.; Bell, I.S.; Coveney, P.I. Simulation of layered double hydroxide intercalates. *Adv. Mater.* **1997**, *9*, 496–500.
42. Yun, S.K.; Pinnavaia, T.J. Water Content and Particle Texture of Synthetic Hydrotalcite-like Layered Double Hydroxides. *Chem. Mater.* **1995**, *7*, 348–354. [CrossRef]
43. Bottero, J.Y.; Manceau, A.; Villieras, F.; Tchoubar, D. Structure and mechanisms of formation of FeOOH(Cl) polymers. *Langmuir* **1994**, *10*, 316–319. [CrossRef]
44. Ferreira Da Rosa, P.P.; Miyazaki, S.; Sakamoto, H.; Kitagawa, Y.; Miyata, K.; Akama, T.; Kobayashi, M.; Fushimi, K.; Onda, K.; Taketsugu, T.; et al. Coordination geometrical effect on ligand-to-metal charge transfer-dependent energy transfer processes of luminescent Eu(III) complexes. *J. Phys. Chem. A* **2021**, *125*, 209–217. [CrossRef] [PubMed]
45. Agrawal, A.; Johns, R.W.; Milliron, D.J. Control of localized surface plasmon resonances in metal oxide nanocrystals. *Annu. Rev. Mater. Res.* **2017**, *47*, 1–31. [CrossRef]
46. Wang, P.X.; Najarian, A.M.; Hao, Z.; Johnston, A.; Voznyy, O.; Hoogland, S.; Sargent, E.H. Structural distortion and bandgap increase of two-dimensional perovskites induced by trifluoromethyl substitution on spacer cations. *J. Phys. Chem. Lett.* **2020**, *11*, 10144–10149. [CrossRef] [PubMed]
47. Oksenberg, E.; Merdasa, A.; Houben, L.; Kaplan-Ashiri, I.; Rothman, A.; Scheblykin, I.G.; Unger, E.L.; Joselevich, E. Large lattice distortions and size-dependent bandgap modulation in epitaxial halide perovskite nanowires. *Nat. Commun.* **2020**, *11*, 489. [CrossRef] [PubMed]

48. Baskoutas, S.; Terzis, A.F. Size-dependent band gap of colloidal quantum dots. *J. Appl. Phys.* **2006**, *99*. [CrossRef]
49. Verma, A.S. An empirical model for bulk modulus and cohesive energy of rocksalt-, zincblende- and chalcopyrite-structured solids. *Phys. Status Solidi Basic Res.* **2009**, *246*, 345–353. [CrossRef]
50. Lin, K.F.; Cheng, H.M.; Hsu, H.C.; Lin, L.J.; Hsieh, W.F. Band gap variation of size-controlled ZnO quantum dots synthesized by sol-gel method. *Chem. Phys. Lett.* **2005**, *409*, 208–211. [CrossRef]
51. Chang, M.C. The electronic states of $Ba_{1-x}Ca_xTiO_3$ and $BaTi_{1-y}Ca_yO_3$ crystalline ceramics. *J. Mater. Sci. Lett.* **2001**, *6*, 237–239. [CrossRef]
52. Sowrey, F.E.; Skipper, L.J.; Pickup, D.M.; Drake, K.O.; Lin, Z.; Smith, M.E.; Newport, R.J. Systematic empirical analysis of calcium-oxygen coordination environment by calcium K-edge XANES. *Phys. Chem. Chem. Phys.* **2004**, *6*, 188–192. [CrossRef]
53. Hao, X.; Tan, L.; Xu, Y.; Wang, Z.; Wang, X.; Bai, S.; Ning, C.; Zhao, J.; Zhao, Y.; Song, Y.F. Engineering active Ni sites in ternary layered double hydroxide nanosheets for a highly selective photoreduction of CO_2 to CH_4 under irradiation above 500 nm. *Ind. Eng. Chem. Res.* **2020**, *59*, 3008–3015. [CrossRef]